International Journal of Engineering Research for Sustainable Development
Peer Reviewed International, Open Access Journal.
ISSN : 3067-2325 / Website: https://ijersd.com / Volume 2 /Issue 3 / June 2026

Original Article

Comparative Study of Bi^{3+}-Substituted Copper Ferrite Using Scherrer, Williamson-Hall, and Halder-Wagner Methods

Tanay S. Gore
Dnyanopasak Shikshan Mandal's Arts, Commerce and Science College, Parbhani, India
School of Physical Sciences, SRTM University, Nanded, India

Manuscript ID:
IJERSD-2026-020301

ISSN: 3067-2325

Volume 2

Issue 3

Pp. 1-9

June 2026

Submitted: 12 May 2026

Revised: 19 May 2026

Accepted: 12 June 2026

Published: 30 June 2026

Correspondence Address:
Tanay S. Gore
Dnyanopasak Shikshan Mandal's Arts, Commerce and Science College, Parbhani, India
School of Physical Sciences, SRTM University, Nanded, India
Email: goretanay@gmail.com

Quick Response Code:

Web. https://rlgjaar.com

DOI: 10.5281/zenodo.21422809

DOI Link:
https://doi.org/10.5281/zenodo.21422809

Abstract

The Bi^{3+}-doped copper ferrite ($CuFe_2O_4$) nanoparticles synthesized via the sol-gel technique using nitrate precursors were extensively examined. The study included advanced characterization techniques to examine structural, elemental, and morphological aspects. The structural phase and crystallinity were determined using X-ray diffraction (XRD), whereas elemental mapping was acquired by Energy Dispersive X-ray analysis (EDX). The nanoparticles' morphology and fine structure were elucidated by High-resolution Transmission Electron Microscopy (HR-TEM). The study utilized peak broadening analysis from XRD and employed various analytical techniques, including the Williamson-Hall (W-H), Size-Strain Plot (SSP), and Halder-Wagner (H-W) methods, to assess crystallite size and lattice strain. These models were compared to ascertain structural factors such as lattice strain and energy density. The particle size was assessed via graphical methods, including Scanning Electron Microscopy (SEM) and High-Resolution Transmission Electron Microscopy (HR-TEM), facilitating a comparison with the results of the W-H, SSP, and H-W methodologies. The findings indicated that the produced nanoparticles exhibited an average particle size ranging from 69 to 77 nm. This multi-method approach elucidates the material's potential applications by emphasizing the intricate interactions among synthesis techniques, structural attributes, and particle dimensions.

Keywords: *Lattice strain; Jahn-Teller (J-T) effect, tetragonal & orthorhombic phase; Crystallite size*

Introduction

New researchers are fascinated by the inherent properties of nanoferrites, which have been widely applied across several technologies over the past three decades. The bulk of investigated ferrites display spinel and tetragonal structures, which significantly affect their magnetic, optical, electrical, and electrochemical properties. The materials' properties can be altered by adding other chemicals, altering the chemical composition, adjusting the manufacturing process, or applying heat. Ferrite nanoparticles are used in various applications, including microwave absorbers, sensors, energy storage systems, drug therapy, magnetic resonance imaging, magnetocaloric refrigerators, and supercapacitors [1-7]. Copper ferrite nanoparticles (CFNs) ($CuFe_2O_4$) are extensively researched ferrites characterized by a cubic spinel structure [8]. However, they do not conform to the typical cubic structure, as divalent ions indiscriminately occupy both tetrahedral and octahedral sites rather than solely tetrahedral sites. CFNs exhibit significant sensitivity to temperature and doping levels, which can alter their structure. They may have a tetragonal structure, indicating a tetragonal phase at lower temperatures and a cubic phase at elevated temperatures [9]. Samples sintered at temperatures over 800°C and thereafter cooled gradually tend to remain in a tetragonal phase. The quick cooling to room temperature maintains the cubic phase. Doping and temperature effects impact phase transitions in CFN structures. Ferrite materials exhibit the coexistence of cubic spinel and tetragonal phases. In CFNs, the Jahn-Teller (J-T) distortion, resulting from $3d^9$ Cu^{2+} ions occupying octahedral sites, induces these structural alterations [10]. The tetrahedral site occupancy of Fe^{3+} and Cu^{2+} ions further diminish magnetic moments, thereby enhancing the Jahn-Teller effect. The J-T effect in the material is controlled by the distribution of Cu^{2+} ions across different sites, the presence of oxygen vacancies, and exchange interactions among ions.

The bismuth ferrite exhibits two distinct phases: magnetic and electric, with a specific focus on the tuning phase inside the material [11]. The researcher investigates magnetoelectric modulation of magnetism by an electric field in magnetoelectric devices. Bi3+ is an excellent option for magnetoelectric devices operating at ambient temperature. Premium materials employ various effects to regulate domains, switch ferroelectrics, enable electronic domain barriers, couple interfacial exchange, and manage ionic defects for electrical and magnetic applications [12–15].

How to cite this article:

Gore, T. S. (2026). Comparative Study of Bi^{3+}-Substituted Copper Ferrite Using Scherrer, Williamson–Hall, and Halder–Wagner Methods. International Journal of Engineering Research for Sustainable Development, 2(3), 1–9. https://doi.org/10.5281/zenodo.21422809

This study focuses on the examination of phase development and phase transitions, and comparative structural analysis of the material using diverse approaches. The intrinsic properties of the materials, such as crystallite size, lattice strain, and the source of intrinsic strain, stem from the material's composition and the formation of grain boundaries and grains during crystal growth [16]. Lattice strain mostly results from lattice dislocations; however, stacking faults, sinter strains, and triple junction grain boundaries may also contribute. The dimensions of the crystallites are discovered by the extent of peak broadening, whereas the Bragg peak serves to quantify intrinsic strain. The Scherrer method is the predominant technique for determining crystallite size from an XRD peak. Nevertheless, it cannot accurately quantify crystallite size as it fails to account for strain and instrumental effects. The Williamson-Hall method, the Size-Strain Plot, and the Halder-Wagner method are effective for determining lattice strain, intrinsic strain, energy density, and dislocation density in nanomaterials [20, 21]. They can also be used to determine crystallite dimensions.

In this study, we investigate the effects of Bi^{3+} doping on synthesized copper ferrite, employing X-ray diffraction (XRD) for crystallographic analysis to elucidate the nanoparticles' morphology and microstructure. XRD was specifically employed to evaluate phase, crystallite size, strain, and dislocation density by various analytical techniques.

Materials and methods

Material used

The synthesis of bismuth-substituted copper ferrite nanoparticles by using reagents like as hexahydrate cupric nitrate ($Cu(NO_3)_2{\cdot}6H_2O$) from Qualigens, nonahydrate iron nitrate ($Fe(NO_3)_3{\cdot}9H_2O$) from Qualigens, pentahydrate bismuth nitrate ($Bi(NO_3)_3{\cdot}5H_2O$) from Sigma Aldrich, and citric acid monohydrate ($C_6H_8O_7{\cdot}H_2O$) from Merck. All chemicals employed were of analytical grade.

Synthesis of bismuth-doped Copper ferrite nanoparticles

The widely deployed sol-gel combustion technique was employed to synthesize CuBixFe2-xO4 CFNs nanoparticles, where x ranges from 0.0 to 1.0. The first step involved carefully weighing all precursors according to their chemical compositions. The subsequent stage involved combining the precursors in various beakers. Bismuth nitrate was combined with nitric acid, while the other precursors were dissolved in deionized water. The third phase involved combining all the compounds and adjusting the solution's pH to 7. The liquid gradually transformed into a gel under prolonged heating. It gradually became denser. As the water molecules evaporated, the viscous gel ultimately ignited and transformed into a powder. The powder was ultimately heated to 550°C for 6 hours.

Characterizations

The structural assessment of the produced Bi3+-doped CuFe2O4 nanoparticle was conducted using Rigaku XRD equipment with a 0.02 step size and a scanning range of 10 to 70 degrees. The radiation source was Cu Kα (1.5406 Å), and the accelerating voltage was 40 kV at 50 mA. The morphological investigation of a sample scanned by scanning electron microscope (SEM, ZEISS Gemini 450). Transmission electron microscopy (TEM) images (JEOL-JEM 2100 Plus) acquired at 200 kV were used to investigate high-resolution surface morphologies, crystallinity, particle size distribution, and lattice spacing. Samples for HRTEM analysis were prepared by dispersing the powder in ethanol and drop-casting onto a 400-mesh Cu grid.

Result and discussion

XRD data analysis

The lattice parameter, crystallite size, and microstrain were the primary parameters examined in the XRD study. At X = 0.0, prominent and pronounced peaks were seen at 2θ angles of 18.37, 30.11, 34.65, 36.22, 44.16, and 62.22. These peaks correspond to the (101), (112), (103), (211), (202), (004), (220), (312), (321), (224), and (400) planes, which match the standard database JCPDS Card no. (48-1548) for a tetragonal crystal structure with the I41/amd space group [31]. The XRD spectra show a single phase of copper ferrite, accompanied by minor secondary peaks. The Bragg peaks at 33.31°, 38.73°, and 54.26° with modest intensity indicate distortion in the tetragonal phase. The Jahn-Teller (J-T) effect, occurring in tetragonal and cubic spinel structures, induces these alterations in copper ferrite [32]. The J-T effect in copper ferrite is mostly associated with Cu^{2+} ions located at octahedral sites, which exhibit significant temperature sensitivity and are formed during the formation process [33]. In copper ferrite, Cu2+ and Fe2+ ions partially occupy the tetrahedral (A-site), whereas Fe3+ and specific Cu2+ ions partially occupy the octahedral (B-site). The material possesses an inverse or mixed spinel configuration. Cu2+ ions predominantly occupy octahedral sites, while they may also partially occupy tetrahedral sites, contingent upon the synthesis method of the material. The Jahn-Teller (J-T) effect refers to a distortion in the geometry of a molecule or crystal that increases its energy stability by lowering its symmetry. The principal factor underlying this occurrence in copper ferrite is the presence of Cu2+ ions, characterized by an electronic configuration of 3d9. Cu2+ ions occupying octahedral sites exhibit an asymmetrical distribution of their d-electrons in the d x2 and dx2-y2 orbitals [35]. The absence of symmetry elongates the octahedron, hence reducing the system's energy. The J-T effect induces alterations in the crystal lattice configuration, potentially resulting in phase transitions among cubic, tetragonal, and orthorhombic structures, contingent upon the quantity and distribution of Cu2+ ions. The J-T distortion in copper ferrite stabilizes the Cu2+ ions and significantly alters the material's physical and magnetic properties [38].

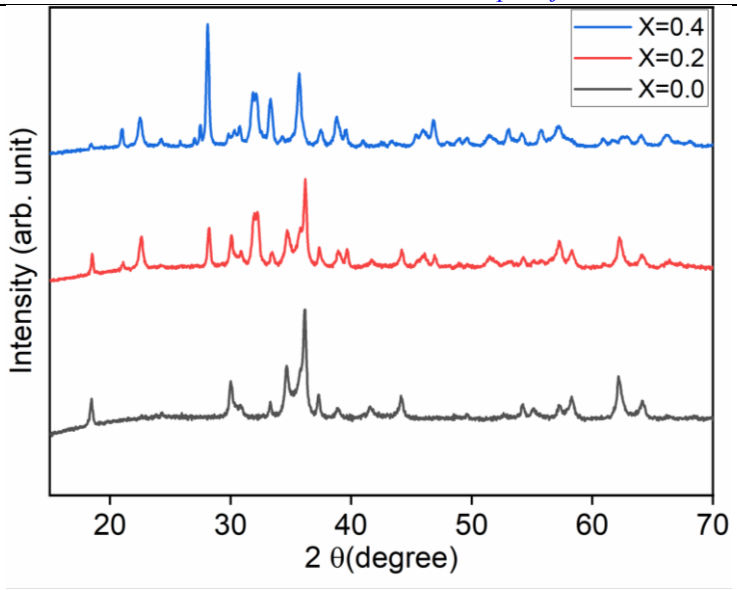

Fig. 1. X-ray diffraction pattern for Bi^{3+} doped $CuFe_2O_4$ synthesized by sol-gel method.

In gas-sensing applications, distortion alters the electrical configuration of the surface, thereby enhancing the reactivity of copper ferrite [39]. The J-T distortion diminishes superexchange interactions in magnetic applications, resulting in reduced magnetic moments and anisotropy [40, 41]. The diffraction data for X = 0.2 and 0.4 exhibited prominent peaks at 2θ angles of 18.46, 22.48, 28.1, 31.86, 33.32, 35.68, 46.8, and 57.22. The peaks correspond to the (002), (020), (112), (022), (212), (041), and (141) planes, indicating that the structure is orthorhombic with the Pbam space group [42]. The incorporation of Bi^{3+} into copper ferrite results in the formation of a novel orthorhombic phase alongside the pre-existing tetragonal phase. At a substitution level of x = 0.2, orthorhombic peaks begin to emerge, while the tetragonal phase remains predominant. However, as the Bi^{3+} concentration increases to x = 0.4, the orthorhombic phase predominates. The (112) plane at 28.1° represents the most pronounced peak, exhibiting a relative intensity of 100%. The biphasic coexistence at x = 0.4 indicates a phase transition driven by two primary factors: the Jahn-Teller (J-T) effect, which involves significant deformation of Cu^{2+} ions in octahedral sites, thereby influencing the lattice structure. The larger ionic radius of Bi^{3+} prevents its incorporation into the tetragonal lattice of copper ferrite, hence maintaining the stability of the orthorhombic phase. This phase transition corresponds to previous research that reported analogous behavior in cobalt ferrite under comparable substitution conditions [43].

In a tetragonal crystal structure, the unit cell lattice parameters are a = b ≠ c, with α = β = γ = 90°. Two lattice parameters are required to fully elucidate its behavior. The d-spacing for the tetragonal crystal structure is determined by using equation 1.

$$\frac{1}{d^2} = \frac{h^2+k^2}{a^2} + \frac{l^2}{c^2} \quad (1)$$

Where h, k, and l are lattice planes.

Table 1 presents the lattice parameters, cell volumes, and c/a ratios for x values of 0.0, 0.2, and 0.4. Upon the addition of Bi^{3+}, the lattice parameter '*a*' increases, whilst the '*c*' parameter decreases. Bi^{3+} possesses a significantly larger ionic radius (1.71 Å) compared to Cu^{2+} (0.73 Å) and Fe^{3+} (0.645 Å). In the tetragonal lattice, Bi^{3+} ions preferentially occupy tetrahedral positions, whereas Cu^{2+} ions preferentially occupy octahedral sites. Nonetheless, the majority of these ions are located on the octahedral B-site. The larger ionic radius of Bi^{3+} enlarges the lattice in the ab-plane, resulting in an increased a-parameter. This induces stress in the lattice along the c-axis, resulting in a reduction of the c-parameter. Cu^{2+} ions exhibit a pronounced Jahn-Teller effect at the octahedral B-site; however, when Bi^{3+} substitutes for them, the Jahn-Teller distortion is diminished due to the absence of this effect in Bi^{3+}. This reduces the c-parameter when the octahedra elongate. The increase in the a-parameter may be attributed to the redistribution of lattice stress inside the ab-plane and the effect of Bi^{3+} substitution on the lengths of the metal-oxygen bonds in this plane. The unit cell (V) for tetragonal Bi3+-doped CuFe2O4 nanoparticles is expressed as $V = a^2c$. To determine the unit cell volume of CFNs, it is essential to ascertain the unit cell lattice parameters a, b, and c. The calculated unit cell volume for the samples ranges from 293.002 to 298.797 Å3, indicating an increase in volume with Bi3+ doping.

Table 1. The lattice constants "a," "c," and cell volume (V) for $CuBi_xFe_{2-x}O_4$ exhibiting a tetragonal unit cell.

Composition (x)	a (Å)	c (Å)	V (Å^3)	c/a
0.0	5.81	8.68	293.002	1.493
0.2	5.83	8.67	293.674	1.487
0.4	5.95	8.44	298.797	1.418

We analyzed the crystallite size, micro-strain, and additional structural properties from the XRD data using the Scherrer technique, Williamson-Hall, and Halder-Wagner methods.

Scherrer equation for determining crystallite size

Paul Scherrer elucidated the correlation between crystallite size and the full width at half maximum (FWHM) of a diffraction peak. This is now referred to as the Scherrer equation for determining crystallite size. When X-rays interact with the substance, the XRD diffraction pattern produces distinct peaks. The peaks are responsible for the instrumental and physical broadening [44, 45]. Utilizing the full width of the peak at half maximum (FWHM) of the diffraction pattern, the physical and

experimental widths of the sample are determined. The FWHM can also be used to determine the crystallite dimensions in the material. Equation 3 presents the Scherrer formula for determining crystallite size.

$$t = \frac{k\lambda}{Cos\theta\beta} \quad 3$$

$$\frac{Cos\theta}{\lambda} = \frac{k}{t.\beta} \quad 4$$

In this equation, t represents the crystallite size, k is a constant (k = 0.94), λ is the wavelength of X-ray radiation, β is the FWHM of the intense peak, and θ is the diffraction angle of the peak. We employed the Scherrer equation [46–48] to determine crystallite sizes by graphical or mathematical analysis. The graphical approach entails plotting cosθ/λ versus 1/β, as illustrated in Fig. 2(a). The Scherrer method indicates that the crystallite sizes vary from 69 to 74 nm, as presented in Table 2.

The Williamson-Hall method

Several factors influence the development and size of crystals. These factors influence the rate of crystal formation, crystal purity, and crystal morphology. Nanocrystalline materials, characterized by structural flaws and a high surface-to-volume ratio, exhibit intrinsic strain. The intrinsic strain influences the mechanical, electrical, thermal, and optical properties of nanocrystals [49, 50]. Intrinsic strain arises from several defects, including grain boundary strain, point defects such as vacancies and interstitial atoms, sintering stress, triple junction strain, stacking fault strain, and coherency stress. The Williamson-Hall method, Warren-Averbach analysis, Balzar and Enzo analysis, Halder-Wagner technique, and size-strain plot are distinct methodologies for examining a material's microstructural characteristics. The Williamson-Hall method is the most effective means to determine both the crystallite size and the intrinsic strain [51–53].

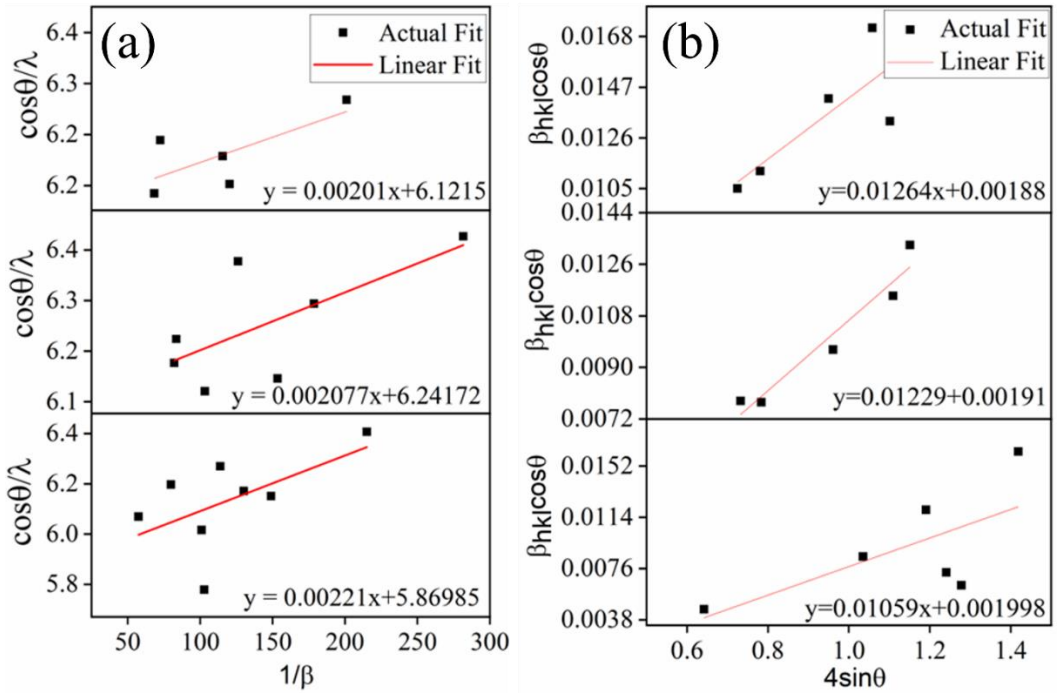

Fig. 2 Crystallite size for x = 0.0,0.2 and 0.4. by (a) Scherrer method (b) Uniform Deformation Model (UDM)

The total peak broadening of the diffraction pattern results from two types of broadening: size broadening and strain broadening. This can be represented by Equation 4:

$$\beta_{total} = \beta_{size} + \beta_{strain} \quad 5$$

Where β_{size} represents the size broadening be contingent on $\frac{1}{cos\theta}$ and β_{strain} represents strain broadening contingent on tanθ. The equation for broadening on size and strain is represented as follows in equations 6 and 7.

$$\beta_{size} = \frac{k\lambda}{t.Cos\theta} \quad 6$$

$$\beta_{strain} = 4\varepsilon.tan\theta \quad 7$$

$$\beta_{total} = \frac{k\lambda}{t.Cos\theta} + 4\varepsilon.tan\theta \quad 8$$

Equation 8 shows how the intrinsic strain (ε) and crystallite size (t) have both gotten bigger. This equation can be used to find lattice deformation stress and uniform strain. The Uniform Deformation Model (UDM), which assumes that the strain is the same throughout the crystal, and the Uniform Stress Deformation Model (USDM), which takes into consideration that the stress is the same across the crystal lattice, are two more versions of the Williamson-Hall model.

Uniform Deformation Model (UDM)

The primary objective of the Uniform Deformation Model (UDM) is to examine the inherent strain induced by crystal defects in a nanocrystal. Uniform strain indicates that the crystal is homogeneous across all orientations (hkl). Uniform strain is a type of deformation that is consistently distributed throughout the entire crystal or material, with minimal variation across regions. In nanocrystals or crystalline materials, uniform strain typically arises from imperfections such as point defects, dislocations, or lattice defects. This model provides both the crystallite dimensions and the crystal's inherent strain. Table 2 presents the crystallite size (t in nm), strain (ε), dislocation density (δ), and specific surface area (in cm^2/g) for Bi3+-doped copper ferrite with X values of 0.0, 0.2, and 0.4.

Parameters	Method/Sample	X = 0.0	X = 0.2	X = 0.4
Crystallite size (t)	SEM	76.14	83.43	85.21
	HR- TEM	71.24	-	-
	Scherrer method	69.71	74.17	76.64
	Uniform Deformation Model (UDF)	72.48	75.82	77.03
	Size-Strain Plot (SSP)	73.13	76.94	86.11
	Halder-Wagner Method	69.97	74.01	77.70
Strain (ε)	Uniform Deformation Model (UDF)	$2.6475x10^{-3}$	$3.0725x10^{-3}$	$3.16x10^{-3}$
	Size-Strain Plot (SSP)	$21.288x10^{-3}$	$8.68638x10^{-3}$	$22.0503x10^{-3}$
	Halder-Wagner Method	$8.695x10^{-2}$	$3.376x10^{-2}$	$19.92x10^{-2}$
Dislocation density (lines/m^{-2})	Williamson and Smallman	$2.042x10^{14}$	$1.825x10^{14}$	$1.656x10^{14}$
Specific surface area (cm^2/gm)	Sauter's SSA	$2.14x10^{11}$	$2.07x10^{11}$	$2.57x10^{11}$

The strain associated with the crystal can be expressed by equation 9.

$$\varepsilon = \frac{\beta}{4\tan\theta} \quad 9$$

$$\beta = \varepsilon\, 4\tan\theta \quad 10$$

Equations 9 and 10 give strain and size broadening in the crystal and the total broadening of the crystal is given by the Williamson-Hall equation as follows.

$$\beta_{hkl} = \frac{k\lambda}{t.}\,\frac{1}{\cos\theta} + 4\varepsilon\,\tan\theta \quad 11$$

Where the total peak broadening at the full width at half maximum (FWHM) of the diffraction pattern can be related to the crystallite size and the intrinsic strain in the crystal.

The broadening of diffraction peaks is caused by two main factors: the crystallite size (t) and intrinsic strain (ε). The total peak broadening (β_{total}) is a combination of these two contributions, which can be expressed as: $\beta_{total} = \beta_{hkl} = \beta_{size} + \beta_{strain}$

Equation 11 can be rearranged in the following way

$$\beta_{hkl}\cos\theta = \frac{k\lambda}{t} + 4\varepsilon\,\sin\theta \quad 12$$

Equation (12) delineates a linear relationship referred to as the Uniform Deformation Model (UDM), predicated on the premise that the crystals exhibit isotropic behavior. The equation above produces the plot in Figure 2(b), with 4sinθ on the X-axis and βhklcosθ on the Y-axis for each diffraction peak of CFNs nanoparticles. Utilize the formula t = kλ/ and the graph's intercept (C) to determine the dimensions of the crystallite (t). Table 2 indicates that the crystallite size ranges from 72.48 nm to 75.82 nm. Figure 2(b) illustrates the intrinsic strain as a linear representation. The observed lattice strain demonstrates that the structure expands and contracts because of its diminutive size. This influences the arrangement of atoms with reference to the bulk material. This limitation diminishes the strength and perfection of the crystal lattice. The UDM diagram indicates that the lattice strain is positive, signifying an expansion of the lattice. The intrinsic strain may range from 2.6475x10^-3 to 3.16x10^-3, contingent upon the slope. The crystal lattice expands and alters its configuration upon the incorporation of larger Bi^{3+} ions. This induces tension on the lattice. The strain may vary based on the quantity and distribution of Bi^{3+} ions within the material. Incorporating Bi^{3+} into the $CuFe_2O_4$ structure can create vacancies and other structural challenges that maintain charge neutrality. These flaws induce deformation in the crystal lattice at certain points, hence influencing the tension within the lattice. The Bi^{3+} ions may exhibit uneven distribution inside the lattice. If doping is uneven, it may result in regions of elevated strain. This may result in a variation in the average strain value for the entire material.

The Size-Strain Plot (SSP) examines peak broadening in X-ray diffraction (XRD) data to ascertain crystallite size and lattice strain. It exceeds the Williamson-Hall approach by utilizing both Gaussian and Lorentzian functions. The Gaussian function signifies strain widening, whereas the Lorentzian function illustrates size broadening. SSP reduces instrument-induced mistakes and eradicates substantial inaccuracies linked to Williamson-Hall or Scherrer's methods. Operates efficiently on low-angle peaks, rendering it appropriate for materials that can endure substantial stress. It facilitates concurrent estimate of size and strain with minimized assumptions, which is beneficial for materials displaying intricate widening profiles. SSP is a reliable technique for assessing particle size and micro-strain, especially when both elements influence peak broadening in XRD. The elaboration of the strain-size methodology can be expressed as follows:

$$\beta_{hkl} = \beta_L + \beta_G \quad 13$$

Where β_L is the peak broadening of the Lorentz function and β_G is the peak broadening of the Gaussian function.

The Size-strain plot analysis can be performed using the following equation [54, 55]

$$(d_{hkl}\,\beta_{hkl}\cos\theta)^2 = \frac{k\lambda}{t}\left(d_{hkl}^2\,\beta_{hkl}\cos\theta\right) + \frac{\varepsilon^2}{4} \quad 14$$

Where d_{hkl} is the lattice distance between planes in a tetragonal crystal,

The formula for the lattice distance d_{hkl} between planes in a tetragonal crystal is:

$$d_{hkl} = \frac{1}{\sqrt{\frac{h^2+k^2}{a^2}+\frac{l^2}{c^2}}} \quad 15$$

The Miller indices of the crystal plane are h, k, and l. The lattice constant along the x- and y-axes is a, and the lattice constant along the z-axis is c. Figure 3 (a) shows the graph of (d_hkl^2 β_hkl cosθ) on the x-axis and (d_(hkl) β_hkl cosθ)^2 on the y-axis using equation 14. Use linear regression to get the best line that fits the data: Y = mx + C. The linear fit gives us the slope (m) and the intercept (C). To find the crystallite size (t) from the slope (m), use the formula t = kλ/m. To find the micro-strain (ε) from the intercept (C), use the formula ε = √4C. The straight-line slope for x = 0.0, 0.2, and 0.4 gives crystallite sizes of

73.13, 76.94, and 86.11 nm, respectively. The Y-intercept shows the material's intrinsic strain, which is measured for x=0.0, 0.2, and 0.4 as 21.288x10-3, 8.68638x10-3, and 22.0503x10-3, respectively.

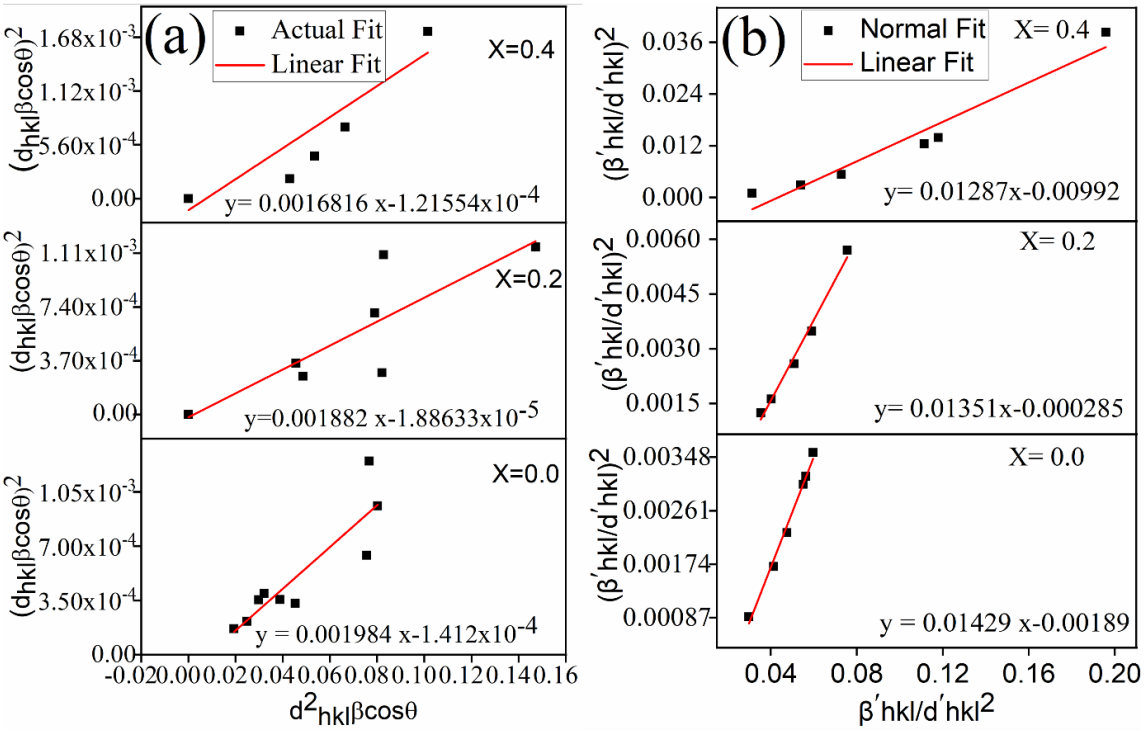

Fig. 3 Crystallite size and Lattice strain by (a) Strain-size method (b) Halder-Wagner Method

The Halder-Wagner Method

The Size-Strain Plot (SSP) approach uses a Lorentzian function to show how size causes the XRD peak profile to spread out, and a Gaussian function to show how strain causes it to spread out. But the real XRD peak profile doesn't quite follow either of these functions. The middle of the XRD peak line up closely with the Gaussian function, but the tailpiece goes down too quickly, therefore it doesn't match. The Lorentzian function performs a good job of representing the tails of the profile, but it doesn't do a good job of capturing the middle peak region. The Halder-Wagner technique is used, which assumes that peak broadening follows a Voigt function that is symmetric. The Voigt function is a mix of the Lorentzian and Gaussian functions. The Halder-Wagner approach says that the full width at half maximum (FWHM) of the physical profile can be written as follows:

$$\beta_{hkl}^2 = \beta_L.\beta_{hkl} + \beta_G^2 \quad (16)$$

In this situation, βL is the full width at half maximum (FWHM) of the Lorentzian part, and βG is the full width at half maximum (FWHM) of the Gaussian part. One excellent thing about this method is that it lends more weight to peaks in the low- and mid-angle areas, where diffraction peaks don't mix too much. The Halder-Wagner method reveals how the size of the crystallites and the strain on the lattice are connected, as seen in [56, 57]:

$$\left(\frac{\beta'_{hkl}}{d'_{hkl}}\right)^2 = \frac{1}{t}\frac{\beta'_{hkl}}{d'^2_{hkl}} + \left(\frac{\varepsilon}{2}\right)^2 \quad (17)$$

Where, $\beta'_{hkl} = \beta_{hkl}\cos\theta/\lambda$ and $d'_{hkl} = 2d_{hkl}\sin\theta/\lambda$.

Equation 17 represents a straight line where 1/t represents slope (M) so the crystallite size t is reciprocal of slope (1/M) and the y-intercept (C) is $(\varepsilon/2)^2$ so the micro-strain (ε) can be obtained from intercept as $2\sqrt{C}$. A graph of equation (17), with the term β'_{hkl}/d'^2_{hkl} on the X-axis and $\left(\frac{\beta'_{hkl}}{d'_{hkl}}\right)^2$ on the Y-axis for each peak in the XRD pattern, is illustrated in Fig. 3(b). The slope of the resulting straight line corresponds to the average crystallite size, while the intercept represents the intrinsic strain in the Bi^{3+} doped $CuFe_2O_4$ nanocrystals. From the plot, the average particle size is calculated to be 69.97 to 77.07 nm, which aligns closely with the value obtained using the SSP model as presented in Table 2. The strain calculated from the Halder-Wagner plot varies from 8.6948×10^{-2} to 19.9194×10^{-2}.

Dislocation density (δ)

The dislocation density for Bi^{3+} doped $CuFe_2O_4$ nanocrystals was obtained by the formula provided by Williamson and Smallman and is expressed as follows [58]:

$$\delta = \frac{1}{t^2} \quad (18)$$

The calculated dislocation density (δ) of Bi3+-doped CuFe2O4 varies from 2.04 × 10^14 to 1.65 × 10^14 lines/m². The variation in dislocation density may be attributed to the manufacturing process, doping, or the material's structural configuration. Increased Bi3+ incorporation can augment lattice strain and crystallite size, resulting in structural defects and heightened dislocation density. The dislocation density decreases as crystallite size increases, hence imposing greater stress on the copper ferrite structure. The alteration in dislocation density is likely attributable to a confluence of variations in crystallite size, lattice strain, and synthesis conditions influenced by Bi3+ doping.

Specific surface area

The specific surface area (SSA) of a material is an essential parameter that defines its chemical reactivity, adsorption potential, role in heterogeneous catalysis, and other surface-dependent reactions. Materials with high specific surface area (SSA)

values generally exhibit increased reactivity. The computation of Sauter's specific surface area can be executed utilizing the following formula [59].

$$S=\frac{6 \times 10^3}{t \times \rho} \quad 19$$

To find the surface area of nanoparticles, utilize the Sauter-specific surface area (SSA) formula. In this case, t is the average size of the crystallites, and ρ is the bulk density of Bi3+-doped copper ferrite, which is measured in g/cm³. The SSA for the produced Bi3+ doped CuFe2O4 nanoparticles was determined to be between 3.43×1011 and 2.57x1011 cm2/g, as shown in Table 2.

We used X-ray diffraction (XRD) peak broadening analysis to look at the size of the particles and the strain that was already in the Bi3+ doped copper ferrite nanoparticles. The analysis utilized the Williamson–Hall (W-H) approach, the Size–Strain Plot (SSP), and the Halder–Wagner (H-W) method. The Uniform Deformation Model (UDM) was also used. These models looked at physical and microstructural factors as strain, stress, and energy density.

Conclusions

The copper ferrite samples were efficiently synthesized by the sol-gel autocombustion method. The pristine copper ferrite indicates a single tetragonal phase, while the bismuth-substituted sample shows phase change to an orthorhombic phase. The change in structure increases the lattice parameter and crystal size. The TEM image indicates a crystallite size of 69-76 nm for the material. The crystallite sizes obtained from the Williamson-Hall, Size-Strain Plot, and Halder-Wagner methods are also matched with the TEM analysis. The Halder-Wagner method yielded lower strain readings compared to the other two techniques. Bi^{3+} doping significantly enhances the material's structure and morphology, potentially rendering it advantageous for gas-sensing applications. The superior lattice properties and dual-phase architecture can alter electrical and catalytic performance, rendering these nanoparticles suitable for environmental monitoring and industrial gas-sensing applications. A subsequent study may examine the functional properties of these materials to enhance their effectiveness in specific applications. Bi^{3+}-doped $CuFe_2O_4$ is a promising multifunctional material for gas-sensing and high-performance energy-storage applications.

Acknowledgment

The authors sincerely acknowledge the Department of Physics, Dnyanopasak Shikshan Mandal's Arts, Commerce and Science College, Parbhani, and the School of Physical Sciences, Swami Ramanand Teerth Marathwada University, Nanded, for providing the necessary academic support and research facilities to carry out this work. The authors are grateful to the laboratories and technical staff who assisted with X-ray diffraction (XRD), SEM, HR-TEM, and EDX characterization. The authors also thank their colleagues and reviewers for their valuable suggestions, which helped improve the quality of this manuscript.

Conflict of Interest: The authors declare that they have no conflict of interest.

Funding: This research did not receive any specific grant from funding agencies in the public, commercial, or not-for-profit sectors.

References:

1. Rohith, S., Radhakrishnan, K., Dinesh, A. et al. Review on the Recent Developments in Magnetic Nanocomposites for Energy Storage Applications. Semiconductors 59, 91–114 (2025). https://doi.org/10.1134/S106378262460219X
2. Shaat, S., Dawoud, H. Influence of variation of structural parameters on magnetic properties of Al-substituted Ni spinel ferrite. J Mater Sci: Mater Electron 32, 11536–11546 (2021). https://doi.org/10.1007/s10854-021-05735-7.
3. Nazia Khatun, Md. Osman Goni, Md.Saidul Islam, Md. Aftab Ali Shaikh, Syed Farid Uddin Farhad, Md. Al-Mamun, Md.Saiful Alam, Nazmul IslamTanvir, Md. Sajjad Hossain, Trisha Paul, Suravi Islam, Impact of lanthanum ions on structural, morphological, magnetic, optical and electrical properties of Cobalt-Zinc ferrites, Journal of Magnetism and Magnetic Materials, Volume 614, 2025, 172740, ISSN 0304-8853, https://doi.org/10.1016/j.jmmm.2024.172740.
4. Chavan, A.R., Khirade, P.P., Somvanshi, S.B. et al. Eco-friendly green synthesis and characterizations of CoFe2-x AlxO4 nanocrystals: analysis of structural, magnetic, electrical, and dielectric properties. J Nanostruct Chem 11, 469–481 (2021). https://doi.org/10.1007/s40097-020-00381-7
5. Undre, P.G., Humbe, A.V., Kounsalye, J.S. et al. Diamagnetic Al3+ Doped Ni–Zn Spinel Ferrite: Rietveld Refinement, Elastic, Magnetic, Mössbauer, and Electrical Explorations. J Inorg Organomet Polym 33, 3372–3388 (2023). https://doi.org/10.1007/s10904-023-02755-0.
6. Jalel Massoudi, Mourad Smari, Kamel Nouric, Essebti Dhahri, Kamel Khirounid, Sylvain Bertainae, Lotfi Bessaisc and El Kebir Hlilf, Magnetic and spectroscopic properties of Ni–Zn–Al ferrite spinel: from the nanoscale to microscale, RSC Adv., 2020, 10, 34556-34580.
7. Nusrat Jahan*Md Nazrul I. KhanJahirul I. KhandakerY, Exploration through Structural, Electrical, and Magnetic Properties of Al3+ Doped Ni–Zn–Co Nanospinel Ferrites, ACS Omega 2021, 6, 48, 32852–32862.
8. Slimani, H. Gunguneş, M. Nawaz, A. Manikandan, H. S. El Sayed, M. A. Almessiere, H. Sozeri, S. E. Shirsath, I. Ercan, A. Baykal, Magneto-optical and microstructural properties of spinel cubic copper ferrites with Li-Al co-substitution, Ceram. Int., 44, 12 (2018) 14242-14250. https://doi.org/10.1016/j.ceramint.2018.05.028.
9. A. M. Balagurov, I. A. Bobrikov, V. Yu. Pomjakushin, D. V. Sheptyakov, V. Yu. Yushankhai, Interplay between structural and magnetic phase transitions in copper ferrite studied with high-resolution neutron diffraction, J. Magn. Mag. Mater., 374, (2015) 591-599. https://doi.org/10.1016/j.jmmm.2014.08.092.
10. M. P. Ghosh, S. Datta, R. Sharma, K. Tanbir, M. Kar, S. Mukherjee, Copper doped nickel ferrite nanoparticles: Jahn-Teller distortion and its effect on microstructural, magnetic and electronic properties, Mater. Sci. Eng. B, 263, (2021) 114864. https://doi.org/10.1016/j.mseb.2020.114864.
11. M. Pooladi, I. Sharifi, M. Behzadipour, A review of the structure, magnetic and electrical properties of bismuth ferrite ($Bi_2Fe_4O_9$), Ceram. Int., 46, 11 (2020) 18453-18463. https://doi.org/10.1016/j.ceramint.2020.04.241.
12. A. Baji, Y. W. Mai, Q. Li, S. C. Wong, Y. Liu, Q. W. Yao, One-dimensional multiferroic bismuth ferrite fibers obtained by electrospinning techniques, Nanotechnology, 22 (2011) 23.
13. S. Prosandeev, Y. Yang, C. Paillard, L. Bellaiche, Displacement Current in Domain Walls of Bismuth Ferrite. npj Comput Mater 4, 8, 2018. https://doi.org/10.1038/s41524-018-0066-y.
14. M. A. K. Budi, E. B. Glass, N. G. Rudawskib, J. S. Andrew, Exchange bias in bismuth ferrite/cobalt ferrite Janus nanofibers, J. Mater. Chem. C, 5 (2017) 8586-8592.

15. A. Molak, D. K. Mahato, A. Z. Szeremeta, Synthesis and characterization of electrical features of bismuth manganite and bismuth ferrite: effects of doping in cationic and anionic sublattice: Materials for applications, Prog. Crystl. Grow. Charact. Mater., 64, 1 (2018) 1-22. https://doi.org/10.1016/j.pcrysgrow.2018.02.001.
16. S. K. Gore, U. B. Tumberphale, S. S. Jadhav, S. F. Shaikh, A. M. Al-Enizi, A. H. S. Rana, R. N. Khule, S. D. Raut, T. S. Gore, R. S. Mane, Grain and grain boundaries influenced magnetic and dielectric properties of lanthanum-doped copper cadmium ferrites. J Mater Sci: Mater Electron 33 (2022) 7636–7647. https://doi.org/10.1007/s10854-022-07912-8.
17. J. Guo, M. J. Duarte, Y. Zhang, A. Bachmaier, C. Gammer, G. Dehm, R. Pippan, Z. Zhang, Oxygen-mediated deformation and grain refinement in Cu-Fe nanocrystalline alloys, Acta Materialia, 166, (2019) 281-293. https://doi.org/10.1016/j.actamat.2018.12.040.
18. M. Z. Qamar, M. Irfan, M. N. Akhtar, R. T. Rasool, A. Almohammedi, S. Ullah, G. A. Ashraf, M. A. Khan, Influence of Pr-cations on structural, spectral, elemental, and electrical features of Zr2–R type ferrites, Ceram. Int., 50, 13 (2024) 23808-23824. https://doi.org/10.1016/j.ceramint.2024.04.108.
19. Z. I. Radzi, B. Vengadaesvaran, N. A. Rahim, S. R. S. Raihan, Influence of calcination temperature on the structural properties of hydrothermally synthesized LiMn1.5Ni0.5O4 cathode material: a comparative study for calculating crystallite size and lattice strain. Appl. Phys. A, 130 (2024) 647. https://doi.org/10.1007/s00339-024-07784-1.
20. K. Patel, A. Patel, V. P. Jethwa, H. Patel, G. K. Solanki, X-ray diffraction analysis of orthorhombic SnSe nanoparticles by Williamson–Hall, Halder–Wagner and Size–Strain plot methods, Chem. Phy. Impact, 8, (2024) 100547. https://doi.org/10.1016/j.chphi.2024.100547.
21. D. Nath, F. Singh, R. Das, X-ray diffraction analysis by Williamson-Hall, Halder-Wagner and size-strain plot methods of CdSe nanoparticles- a comparative study, Mater. Chem. Phys., 239, (2020) 122021. https://doi.org/10.1016/j.matchemphys.2019.122021.
22. T. M. Gur, Review of electrical energy storage technologies, materials and systems: challenges and prospects for large-scale grid storage, Energy Environ. Sci., 11 (2018) 2696-2767.
23. J. Yan, Q. Wang, T. Wei, Z. Fan, Recent Advances in Design and Fabrication of Electrochemical Supercapacitors with High Energy Densities, Adv. Energy Mater., 4 (2014) 1300816.
24. H. Xiao, S. Yao, H. Liu, F. Qu, X. Zhang, X. Wu, NiO nanosheet assembles for supercapacitor electrode materials, Prog. Natu. Sci. Mater. Int., 26, (2016) 271-275.
25. S. J. Uke, S. P. Mardikar, D. R. Bambole, Y. Kumar, G. N. Chaudhari, Sol-gel citrate synthesized Zn doped $MgFe_2O_4$ nanocrystals: A promising supercapacitor electrode material, Mater. Sci. Ene. Tech., 3, (2020) 446-455.
26. M. Saranya, R. Ramachandran, F. Wang, Graphene-zinc oxide (G-ZnO) nanocomposite for electrochemical supercapacitor applications, J. Sci. Adv. Mater. Dev., 1 (2016) 454-460.
27. S. Grover, P. Kadyan, S. Sharma, K. Sharma, R. K. Sharma, Synthesis and characterization of polyaniline nanotube supported nanocomposite of RuO_2 as electrode material for application in supercapacitor device, Materialia, 28 (2023) 101732.
28. Mohamad Mohsen Momeni, Hossein Mohammadzadeh Aydisheh, Byeong-Kyu Lee, Effectiveness of MnO_2 and V_2O_5 deposition on light fostered supercapacitor performance of $WTiO_2$ nanotube: Novel electrodes for photo-assisted supercapacitors, Chem. Eng. J., 450, (2022) 137941.
29. Y. Guo, Y. Chen, X. Hu, Y. Yao, Z. Li, Tween modified $CuFe_2O_4$ nanoparticles with enhanced supercapacitor performance, Collo. Surf. A: Physicochem. Eng. Asp., 631 (2021) 127676.
30. F. N. Mansoorie, P. Bhatt, A. Tewari, R. Kumar, M. Bag, Unveiling the Impact of Bi^{3+} Heterovalent Doping on the Negative Capacitance and Ionic Conductivity of Perovskite Single Crystals: Implication in Neuromorphic Computing, ACS Appl. Mater. Interfaces, 17 (2025) 4218–4230.
31. K. Rajashekhar, G. Vinod, K. Mahesh Kumar, G. Harikishan, Laxman Naik J, Sm^{3+} induced structural phase transition, spectral, morphological, magnetic, dielectric and impedance properties of $Ni_{0.1}Cu_{0.9}Sm_xFe_{2-x}O_4$ nanoferrites, J. Rare Earths, 41, 11, (2023) 1736-1745. https://doi.org/10.1016/j.jre.2022.09.011.
32. M. P. Ghosh, S. Datta, R. Sharma, K. Tanbir, M. Kar, S. Mukherjee, Copper doped nickel ferrite nanoparticles: Jahn-Teller distortion and its effect on microstructural, magnetic and electronic properties, Mater. Sci. Eng. B, 263, (2021) 114864. https://doi.org/10.1016/j.mseb.2020.114864.
33. K. Wu, Y. Lu, Y. Liu, Y. Liu, M. Shen, M. Debliquy, C. Zhang, Synthesis and acetone sensing properties of copper (Cu^{2+}) substituted zinc ferrite hollow micro-nanospheres, Ceram. Int., 46, 18, (2020) 28835-28843. https://doi.org/10.1016/j.ceramint.2020.08.049.
34. I. B. Bersuker, Pseudo-Jahn–Teller Effect—A Two-State Paradigm in Formation, Deformation, and Transformation of Molecular Systems and Solids, Chem. Rev., 113 (2013) 3. https://doi.org/10.1021/cr300279n.
35. L. Shi, K. Chen, T. Huang, Y. Zhang, Z. Wang, Q. Zhang, Unraveling the role of Cu^{2+} induced Jahn-Teller distortion and electron occupation alternation in modulating electronic and optical properties of $Cu_xFe_{1-x}Fe_2O_4$, Ceram. Int., 50, 3, (2024) 23937-23944. https://doi.org/10.1016/j.ceramint.2024.04.124.
36. R. J. Birgeneau, J. K. Kjems, G. Shirane, L. G. Van Uitert, Cooperative Jahn-Teller phase transition in $PrAlO_3$, Phys. Rev. B. 10, (1974) 2512. DOI: https://doi.org/10.1103/PhysRevB.10.2512.
37. M. Javed, A. A. Khan, N. Akbar, J. Kazmi, M. A. Mohamed, Temperature and frequency dependent response of electrical conduction and dielectric relaxation mechanism in $CuCr_2O_4$ tetragonally distorted spinel chromite, Ceram. Int., 50, 3, (2024) 4767-4781. https://doi.org/10.1016/j.ceramint.2023.11.221.
38. C S. Vandana, B. H. Rudramadevi, Effect of Cu^{2+} substitution on the structural, magnetic and electrical properties of gadolinium orthoferrite, Mater. Res. Exp., 5, (2018) 4.
39. George, J., Abraham, K. E. The structural phase change of copper ferrite and its gas-sensing properties. J Mater Sci: Mater Electron 32, 13220–13238 2021. https://doi.org/10.1007/s10854-021-05869-8.
40. F. Fakhry, E. Shaheen, H. El-Dosoky, T. M. Meaz, M. Mubark, R. El-Shater, Elastic and magnetic characteristics of nano-spinel ferrite $Co_{0.5}M_{gx}Cu_{0.5-x}Fe_2O_4$. Sci. Rep., 14, (2024) 29407. https://doi.org/10.1038/s41598-024-74484-4.
41. A. V. Humbe, J. S. Kounsalye, S. B. Somvanshi, A. Kumar, K. M. Jadhav, Cation distribution, magnetic and hyperfine interaction studies of Ni–Zn spinel ferrites: role of Jahn Teller ion (Cu^{2+}) substitution, Mater. Adv., 1, (2020) 880-890.
42. A. Molak, D. K. Mahato, A. Z. Szeremeta, Synthesis and characterization of electrical features of bismuth manganite and bismuth ferrite: effects of doping in cationic and anionic sublattice: Materials for applications, Prog. Crys. Grow. Char. Mater., 64, 1, (2018) 1-22. https://doi.org/10.1016/j.pcrysgrow.2018.02.001.

43. S. K. Gore, S. S. Jadhav, V. V. Jadhav, S. M. Patange, M. Naushad, R. S. Mane, K. H. Kim, The structural and magnetic properties of dual phase cobalt ferrite. Sci Rep 7, (2017) 2524. https://doi.org/10.1038/s41598-017-02784-z.
44. S. Rani, M. Shekhar, P. Kumar, S. Prasad, Study on quantitative Rietveld analysis of XRD patterns of different sizes of bismuth ferrite. Appl. Phys. A 128, (2022) 1046. https://doi.org/10.1007/s00339-022-06171-y.
45. T. T. N. Nha, D. N. Toan, P. H. Nam, D. H. Manh, D. T. Khan, P. T. Phong, Determine elastic parameters and nanocrystalline size of spinel ferrites MFe_2O_4 (M = Co, Fe, Mn, Zn) through X-ray diffraction and infrared spectrum: Comparative approach, J. Alloy. Comp., 996, (2024) 174773. https://doi.org/10.1016/j.jallcom.2024.174773.
46. S. M. Rathod, S. V. Gaikwad, S. K. Gore, U. B. Tumberphale, S. F. Shaikh, M. Ubaidullah, B. Pandit, S. S. Jadhav, Ni–Ag ferrites synthesized by sol gel route using aloe vera extract as a solvent: Enhancement in structural, dielectric, magnetic and optical properties, Phy. B: Cond. Mat., 661, (2023) 414944. https://doi.org/10.1016/j.physb.2023.414944.
47. A. D. Patil, R. A. Pawar, S. M. Patange, S. S. Jadhav, S. K. Gore, S. E. Shirsath, S. S. Meena, TiO_2-Doped $Ni_{0.4}Cu_{0.3}Zn_{0.3}Fe_2O_4$ Nanoparticles for Enhanced Structural and Magnetic Properties, ACS Omega, 6, 28, (2021) 17931–17940.
48. V. B. Kawade, S. S. Jadhav, S. M. Patange, S. D. Raut, R. N. Khule, U. B. Tumberphale, B. Ghule, S. K. Gore, Structural, Morphological, and Dielectric Evaluation of Co^{2+} Doped Zinc Ferrite Aluminate, Macromolecular Symposia, 400 (2021) 1.
49. P. A. Vinosha, A. Manikandan, R. Ragu, A. Dinesh, K. Thanrasu, Y. Slimani, A. Baykal, B. Xavier, Impact of nickel substitution on structure, magneto-optical, electrical and acoustical properties of cobalt ferrite nanoparticles, J. Alloy. Comp., 857, (2021) 157517. https://doi.org/10.1016/j.jallcom.2020.157517.
50. S. Noreen, A. Hussain, M. B. Tahir, A. B. Ziya, J. U. Rehman, M. Usman, S. A. Khan, S. Akhtar, Structural, mechanical, thermodynamic, electronic, magnetic and optical properties of $ZnFe_2O_4$ ferrite: A DFT study, Opt. Mater., 133, (2022) 112930. https://doi.org/10.1016/j.optmat.2022.112930.
51. S. K. Gore, U. B. Tumberphale, S. S. Jadhav, R.S. Kawale, M. Naushad, R. S. Mane, Microwave-assisted synthesis and magneto-electrical properties of Mg-Zn ferrimagnetic oxide nanostructures, Phys. B: Cond. Mat., 530 (2018) 177-182. https://doi.org/10.1016/j.physb.2017.11.044.
52. S. K. Gore, R. S. Mane, M. Naushad, S. S. Jadhav, M. K. Zate, Z. A. Alothman, B. K. N. Hui, Influence of Bi^{3+}-doping on the magnetic and Mössbauer properties of spinel cobalt ferrite, Dalton Trans., 44 (2015) 6384-6390.
53. R. A. Pawar, S. M. Patange, A. R. Shitre, S. K. Gore, S. S. Jadhav, S. E. Shirsath, Crystal chemistry and single-phase synthesis of Gd^{3+} substituted Co–Zn ferrite nanoparticles for enhanced magnetic properties, RSC Adv., 8 (2018) 25258-25267.
54. M. Basak, M. L. Rahman, M. F. Ahmed, B. Biswas, N. Sharmin, The use of X-ray diffraction peak profile analysis to determine the structural parameters of cobalt ferrite nanoparticles using Debye-Scherrer, Williamson-Hall, Halder-Wagner and Size-strain plot: Different precipitating agent approach, J. Alloy. Comp., 895, 2 (2022) 162694. https://doi.org/10.1016/j.jallcom.2021.162694.
55. K. V. Chandekar, K. M. Kant, Size-strain analysis and elastic properties of $CoFe_2O_4$ nanoplatelets by hydrothermal method, J. Mol. Struct., 1154 (2018) 418-427. https://doi.org/10.1016/j.molstruc.2017.09.104.
56. S. Debnath, R. Das, Cobalt doping on nickel ferrite nanocrystals enhances the micro-structural and magnetic properties: Shows a correlation between them, J. Alloy. Comp., 852 (2021) 156884. https://doi.org/10.1016/j.jallcom.2020.156884.
57. S. A. Hassanzadeh-Tabrizi, Precise calculation of crystallite size of nanomaterials: A review, J. Alloy. Comp., 968, (2023) 171914. https://doi.org/10.1016/j.jallcom.2023.171914.
58. A. Borbely, The modified Williamson-Hall plot and dislocation density evaluation from diffraction peaks, Scri. Mater., 217 (2022) 114768. https://doi.org/10.1016/j.scriptamat.2022.114768.
59. Mubasher, M. Mumtaz, M. Hassan, L. Ali, Z. Ahmad, M. A. Imtiaz, M. F. Aamir, A. Rehman, K. Nadeem, Comparative study of frequency-dependent dielectric properties of ferrites MFe_2O_4 (M = Co, Mg, Cr and Mn) nanoparticles. Appl. Phys. A 126 (2020) 334. https://doi.org/10.1007/s00339-020-03529-y.